

Article

Biomimetic Amorphous Titania Nanoparticles as Ultrasound Responding Agents to Improve Cavitation and ROS Production for Sonodynamic Therapy

Joana C. Matos ^{1,2,3}, Marco Laurenti ⁴ , Veronica Vighetto ⁴, Laura C. J. Pereira ² ,
João Carlos Waerenborgh ² , M. Clara Gonçalves ^{1,3,*} and Valentina Cauda ^{4,*} 

¹ Centro de Química Estrutural, Universidade de Lisboa, Av. Rovisco Pais, IST, 1000 Lisboa, Portugal; joana.matos@tecnico.ulisboa.pt

² Centro de Ciências e Tecnologias Nucleares, Instituto Superior Técnico, Universidade de Lisboa, 2685-066 Bobadela LRS, Portugal; lpereira@ctn.tecnico.ulisboa.pt (L.C.J.P.); jcarlos@ctn.tecnico.ulisboa.pt (J.C.W.)

³ Departamento de Engenharia Química, Instituto Superior Técnico, Universidade de Lisboa, Av. Rovisco Pais, 1000 Lisboa, Portugal

⁴ Department of Applied Science and Technology, Politecnico di Torino, Corso Duca degli Abruzzi 24, 10129 Torino, Italy; marco.laurenti@polito.it (M.L.); veronica.vighetto@polito.it (V.V.)

* Correspondence: clara.goncalves@tecnico.ulisboa.pt (M.C.G.); valentina.cauda@polito.it (V.C.); Tel.: +351-218-419-934 (M.C.G.); +39-011-090-7389 (V.C.)

Received: 8 October 2020; Accepted: 23 November 2020; Published: 27 November 2020



Abstract: Conventional therapies to treat cancer often exhibit low specificity, reducing the efficiency of the treatment and promoting strong side effects. To overcome these drawbacks, new ways to fight cancer cells have been developed so far focusing on nanosystems. Different action mechanisms to fight cancer cells have been explored using nanomaterials, being their remote activation one of the most promising. Photo- and sonodynamic therapies are relatively new approaches that emerged following this idea. These therapies are based on the ability of specific agents to generate highly cytotoxic reactive oxygen species (ROS) by external stimulation with light or ultrasounds (US), respectively. Crystalline (TiO₂) and amorphous titania (a-TiO₂) nanoparticles (NPs) present a set of very interesting characteristics, such as their photo-reactivity, photo stability, and effective bactericidal properties. Their production is inexpensive and easily scalable; they are reusable and demonstrated already to be nontoxic. Therefore, these NPs have been increasingly studied as promising photo- or sonosensitizers to be applied in photodynamic/sonodynamic therapies in the future. However, they suffer from poor colloidal stability in aqueous and biological relevant media. Therefore, various organic and polymer-based coatings have been proposed. In this work, the role of a-TiO₂ based NPs synthesized through a novel, room-temperature, base-catalyzed, sol-gel protocol in the generation of ROS and as an enhancer of acoustic inertial cavitation was evaluated under ultrasound irradiation. A novel biomimetic coating based on double lipidic bilayer, self-assembled on the a-TiO₂-propylamine NPs, is proposed to better stabilize them in water media. The obtained results show that the biomimetic a-TiO₂-propylamine NPs are promising candidates to be US responding agents, since an improvement of the cavitation effect occurs in presence of the developed NPs. Further studies will show their efficacy against cancer cells.

Keywords: sonodynamic therapy; a-TiO₂ based nanoparticles; reactive oxygen species; electron paramagnetic resonance spectroscopy; passive cavitation detection; ultrasounds; self-assembled lipid bilayers

1. Introduction

Cancer is the second leading cause of death worldwide. This disease corresponds to a rapid and uncontrolled abnormal cell growth and can affect any part of the body. Today there are around 100 different types of cancer and an increase of around 70% of cancer types is expected in the next two decades [1–3].

Today cancer therapy strategies lack specificity, thus the development of safer and more efficient systems for chemotherapeutics delivery and/or new treatment methodologies is of great importance. Nanomedicine is an emerging and promising field in the discovery and development of new strategies for cancer treatment. The design and development of novel tailor-made nanosystems allow for accurate strategies to eliminate cancer cells by selective accumulation of systematically administered chemotherapeutics. The leaky vasculature and poor lymphatic drainage of the tumor tissues actually enhance the permeability and retention effects (EPR) [4–7]. In the last decades, extensive research has been accomplished to make the transport of the chemotherapeutic agents even more precise, minimizing the collateral harmful effects on healthy tissues [8–10].

Other new approaches for cancer treatment have appeared with the emergence of stimuli-responsive nanomedicine such as photodynamic (PDT) and sonodynamic (SDT) therapies. In both cases, solid-state nanoparticles are used as the photo- or sonosensitizer, respectively. Both therapies are based on reactive oxygen species (ROS) generation and their ability to kill cancer cells. The ROS are originated by the partial reduction of the molecular oxygen (O_2) into new species, being the hydroxyl radical ($\bullet OH$) the strongest radical ever described [11].

Oxygen is fundamental for the normal metabolic activity of all aerobic organisms, being vital for the correct maintenance of life. However, cellular survival implies the existence of a very strict redox homeostasis equilibrium and any instability may result in different types of diseases [12]. Namely, the excessive production of ROS provokes a disequilibrium in the redox state which may lead to cellular components (proteins, DNA, or lipids) damage. However, these effects, generated by the cellular oxidative stress, are being exploited for the development of new therapeutics for cancer treatment [13,14], for example the PDT and SDT therapies [11].

As stated above, the principle behind the PDT and SDT is the generation of ROS using an external stimulus as ultraviolet (UV) or near-infrared (NIR) light, or low intensity ultrasounds (US), respectively [11]. PDT is based on the ability of a specific molecule or material, i.e., the photosensitizer, to be excited by the absorption of light at specific wavelengths and to generate free radicals. The interaction of the photoexcited sensitizer with molecular oxygen results in the production of ROS such as singlet oxygen, hydroxyl radicals, and superoxide ions. Several classes of materials have been successfully investigated as photosensitizers for PDT including semiconducting nanoparticles [15], porphyrins, and other organic dyes [16]. PDT is however limited to superficial tumors treatment due to the light poor tissue penetration. Generally, the efficient penetration depth for PDT is reported to be up to 1 cm when NIR light sources are used. Although even larger penetration depths for PDT can be obtained with the help of optical fibers [17], this approach is limited to endoscopically reachable tumors. Moreover, PDT relies on the use of light-sensitive therapeutic agents, which prevents patients from sunlight exposure after administering of photosensitizer.

SDT mainly relies on the activation of acoustic cavitation phenomena due to the interaction of the medium with US waves. Ultrasound consists of mechanical pressure waves able to induce the formation and the oscillations of gas microbubbles in the stimulated medium. For particular US operating conditions, the as-formed microbubbles can collapse and locally generate very high pressures and temperatures [18] which allow the formation of ROS. This process can be achieved only by operating above specific conditions (cavitation threshold). The introduction in the medium of specific compounds, i.e., sonosensitizers, can lower this cavitation threshold and favor the formation of ROS, as discussed in the following. The first SDT systems came out in 1989 by Umemura et al. [19] who used the already-known photosensitizer hematoporphyrin as sonosensitizer. Most of the sonosensitizers are organic molecules such as porphyrin derivatives, phthalocyanines

among others [19–21]. However, these molecules are characterized by a high aggregation tendency in physiologic medium, and a minor cancer tissue selectivity, which decreases the therapy effectiveness [21]. The research for more efficient alternatives is in progress, e.g., Harada et al. found that crystalline TiO₂ nanoparticles (NPs) activated by ultrasounds (US) can also work as sonosensitizer to reduce the neoplastic tissue [22].

The above-mentioned compounds chemically react or introduce a large amount of bubbles into a specific medium (by their oscillation and/or their violent collapse) and behave like a chemical nanoreactor, leading to ROS generation [23]. The recognized advantage of SDT over the PDT is its higher tissue penetration, which allows the treatment of tumors located deeply in the body. The use of US in SDT is even manifold [21]. Apart from the well-known US imaging capabilities, it is also generally recognized that the combination of ultrasounds and sonosensitizers also lead to sonochemical reactions additional to cavitation, like sonoluminescence and pyrolysis reactions. These might contribute to a more efficient generation of highly toxic species and, therefore, it might further improve the overall efficacy of SDT treatments [24–26].

Semiconductor crystalline TiO₂ is a very well-known nanomaterial due to its photo-reactivity, photo-stability, and effective bactericidal performance. Crystalline TiO₂ (approved by the American Food and Drug Administration) has been widely used as food additive, as photo-active material in pharmaceutical, dermatological products (like in sunscreens), but also in paints, wastewater/drinking water membranes, in photovoltaic and photocatalytic devices [27–31]. It has also been demonstrated that crystalline TiO₂ is biologically inert in animals and humans, presents a good biocompatibility, and no toxicity in vitro or in vivo [32,33]. For this reason, nanosized titania have found interesting and promising application in cancer therapy and diagnosis, i.e., theranostics [34], and specifically for SDT [35,36].

Recently amorphous-TiO₂ has attracted great interest in the academic community [37–46], where a set of new a-TiO₂ applications have been proved: high performance photocatalysts [38], dye sensitizers [43,46], solar battery electrodes [44,46], sodium ion anodes for rechargeable batteries [45], capacitors thin films [38], resistive random access memories [43], self-cleaning agents and water purifiers (in dye-polluted aqueous systems) [47], dehumidifiers [48], visible light photocatalysts [44], and biomedical devices [49,50]. Some of the authors have proved the bactericidal performance of a-TiO₂ NPs and explained theoretically the amorphous semiconductor performances [51–53].

Furthermore, a-TiO₂ are often the first phases to form in many wet chemical synthetic routes (other times the first nuclei to form are anatase that rapidly evolve to oxy-hydroxy amorphous phases [37]). Amorphous TiO₂ is easy to process into different forms, its reduced order state allows a wide range of possible formulation with high levels of dopants. Furthermore, a-TiO₂ exhibits large surface area populated with many -OH groups and great number of structural defects which enhance the photocatalytic activity.

In a recent review, Bogdan et al. [35] commented on the role of nanosized crystalline semiconductors, like TiO₂ and zinc oxide (ZnO) NPs, in generating oxidative stress to cells, i.e., in terms of ROS generation, and on their potential anticarcinogenic applications. The claimed mechanism is attributed to the role of cavitation bubbles under ultrasound irradiation [35]. The US acoustic wave can induce thermal and nonthermal effects while propagating in a liquid or in a biologic tissue. Thermal effects can be exploited as tumor therapy inducing thermo-ablation of the tissue and are generally addressed with high intensity focused US (HIFU) therapy [21]. Nonthermal effects of the US are responsible for several phenomena, the most prominent constituted by acoustic cavitation [21]. The gases dissolved in the liquid, irradiated by US, form micro-sized bubbles which can expand and shrink according to the US wave cycles. The oscillation of microbubbles on their radius for several cycles refers to stable or noninertial cavitation and can induce temperature increase in tissues, microstreaming, radiation forces, and shear stress. Under certain US conditions, the microbubbles collapse generating very high temperatures, pressures and emission of photons, i.e., sonoluminescent light. This phenomenon is called inertial cavitation and, due to the violent bubble collapse, can induce ROS formation [21].

It has been demonstrated that the presence of NPs can decrease the US dose needed to induce acoustic cavitation [12], since the high surface area of the NPs allows a high adsorption of tiny gas bubbles that will act as nucleation sites for cavitation [54]. Therefore, an increase of the active microbubbles number under the US irradiation is observed and these can be used to induce mechanical and oxidative stress to cells during cancer treatment [55]. Furthermore, the generation of sonoluminescence light was also hypothesized to be responsible in the photoexcitation of semiconducting NPs, like crystalline TiO₂ or ZnO [24], by the promotion of one electron from the valence band (V_B) to the conduction band (C_B), leaving a hole behind. Unpaired electrons and holes can react with oxygen and water molecules (adsorbed at the NPs' surfaces) generating ROS ($\bullet\text{O}_2^-$, $\bullet\text{OH}$, H₂O₂).

In this work, the ability of α -TiO₂-based NPs (both pristine α -TiO₂ and propylamine-functionalized α -TiO₂-NH₂ NPs), synthesized through a novel, room-temperature, base-catalyzed, sol-gel protocol, was evaluated for the first time to work as a sonosensitizer, reducing the cavitation threshold and improving the generation of ROS under US irradiation. An increase in ROS generation was observed in the presence of such α -TiO₂ NPs, either pristine or propylamine functionalized, thus to verify the decreasing limit from which ROS formation occurs due to the ultrasound irradiation. The effect of visible light on ROS generation was also discussed. The results evidenced a synergistic effect between both US and visible light stimuli.

Furthermore, to improve the colloidal stability of the synthesized NPs, aiming for future biological/medical applications, the α -TiO₂-NH₂ NPs were coupled with phospholipids (DOPC-DOTAP). This is an important improvement since the application of α -TiO₂ based NPs in biological systems can be compromised due to their poor colloidal stability in water and/or biological media [49,50,56]. Some of the authors have previously reported the ability to self-assemble phospholipid bilayers on hard inorganic particle surfaces, i.e., mesoporous silica NPs [57], ZnO nanocrystals [58,59], and metal-organic frameworks [60,61]. Thus, we prove here for the first time a similar formulation of phospholipid bilayers on such α -TiO₂ NPs, showing their enhanced colloidal stability in solution and thus a biomimetic behavior which can be further applied to treat cell cultures.

Then, the ability of the biomimetic α -TiO₂ NPs in generating ROS during US stimulation was evaluated through electron paramagnetic resonance (EPR) spectroscopy assisted by a spin-trapping technique. Finally, passive cavitation detection (PCD) was used to verify the presence of cavitation phenomena. The obtained results showed that these lipid coated α -TiO₂ NPs biomimetic NPs can act as promising cavitation enhancers under US irradiation and be applied either in anticancer therapies or other biomedical applications, i.e., antimicrobial effects.

2. Materials and Methods

2.1. Materials

Aqueous sodium silicate solution (SSS; Na₂O.SiO₂, 27% wt. % SiO₂), titanium IV isopropoxide (TiPOT, Ti[OCH(CH₃)₂]₄, 97%), 3-aminopropyltriethoxysilane (APTES; H₂N(CH₂)₃Si(OC₂H₅)₃, 99%) were purchased from Sigma-Aldrich (Darmstadt, Germany).

Absolute ethanol (EtOH; 99.5%) from Merck (Darmstadt, Germany) and bidistilled water (conductivity 0–2 $\mu\text{S}/\text{cm}^3$, pH 5.8–6.5) were also used.

The commercial phospholipids 1,2-dioleoyl-*sn*-glycero-3-phosphocholine (DOPC) and 1,2-dioleoyl-3-trimethylammonium propane (DOTAP) for the biomimetic shielding of α -TiO₂-NH₂ NPs were purchased from Avanti Polar lipids. 3,3'-Diocadecyloxycarbocyanine Perchlorate (DiOC₁₈) and ATTO550-NHS ester fluorescent dyes, purchased from ThermoFischer, were used for fluorescence microscopy colocalization experiments.

All chemicals were used without any further purification.

2.2. Synthesis and Functionalization of *a*-TiO₂ NPs

Amorphous TiO₂ NPs (*a*-TiO₂ NPs) were synthesized through a novel, alkaline, and room temperature sol-gel process based on the protocol previously reported by Matos et al. [51].

Briefly, a volume (280 µL) of sodium silicate solution (SSS) as nucleating agent was diluted in absolute ethanol (25 mL) and placed under magnetic stirring for 15 min. A mixture of absolute ethanol and ammonium hydroxide was added to the suspension and left under magnetic stirring for an additional 15 min. After this time, the suspension was placed in an ultrasound bath (TELSONIC Switzerland, Tec-15, Economy-Cleaner) and 500 µL of titanium isopropoxide (TiPOT) was rapidly added, followed by 30 min of sonication.

The *a*-TiO₂ NPs functionalization was made in situ with propylamine groups following the above methodology. After the 30 min of titanium isopropoxide sonication, a volume of APTES was added in a molar ratio of 8:2 of TiPOT to APTES. The mixture was then left under magnetic stirring for 24 h at room temperature.

2.3. Coupling of *a*-TiO₂-NH₂ NPs with DOPC-DOTAP Lipid

The preparation of lipid-coated NPs (*a*-TiO₂-NH₂//DOPC-DOTAP) was performed through a solvent exchange method. An amount of 1.75 mg of 1,2-dioleoyl-*sn*-glycero-3-phosphocholine (DOPC) and 0.75 mg of 1,2-dioleoyl-3-trimethylammonium propane (DOTAP, positively charged) in chloroform (mass ratio of 70% DOPC and 30% DOTAP) were mixed together and dried under vacuum overnight and redispersed in a 1 mL mixture of 40% (*v/v*) ethanol and 60% (*v/v*) bidistilled water. From the prepared stock solution of DOPC-DOTAP, 100 µL was removed and added to 50 µg of *a*-TiO₂-NH₂ NPs. To induce the self-assembly of the phospholipid bilayer on the titania NPs surface, 900 µL of bidistilled water was added to the previous suspension and vortexed for 5 min. The *a*-TiO₂-NH₂//DOPC-DOTAP NPs were washed twice with bidistilled water to remove the unbound lipids by centrifuging the NPs at 10,000 RCF for 5 min, discarding the supernatant and adding fresh water. For the EPR and PCD experiments, the whole procedure was scaled-up.

To confirm the coupling efficiency between the NPs and lipids, two labeling steps were added before the fluorescence microscopy experiments. The *a*-TiO₂-NH₂ NPs were labeled with ATTO550-NHS ester dye, at a ratio of 2 µg of dye per mg of NPs. The suspension of NPs with dye was kept in the dark under continuous stirring overnight and then the sample was washed twice with fresh ethanol to remove the unbound dye compounds. The lipid bilayer, once already self-assembled on the *a*-TiO₂-based NPs, was labeled with DiOC₁₈ lipophilic carbocyanine dye by adding 0.5 µL of the fluorescent dye to the suspension of NPs//lipids and left in an orbital shaker at 37 °C for 30 min.

2.4. Physico-Chemical Characterization of *a*-TiO₂ Based NPs

2.4.1. Transmission Electron Microscopy (TEM)

The morphology, static diameter, and size distribution of *a*-TiO₂ based NPs were studied by transmission electron microscopy (TEM) [51]. The model used was a Hitachi H-8100, a conventional TEM with high brightness LaB6 electron source and large specimen-tilt (>30°). The micrographs were obtained using an applied tension of 200 kV and the samples were prepared by placing a drop of NPs suspension on a copper grid and dried at room temperature.

2.4.2. X-ray Powder Diffraction (XRD)

The amorphous character of the synthesized NPs was proved by powder X-ray diffraction (XRD) [51]. The analyses were performed by a PANalytical X'Pert Pro diffractometer using Cu-Kα radiation. The data were collected in the 20°–80° 2θ range (step size 0.02°, acquisition time 4 s).

2.4.3. Fourier Transform Infrared (FTIR) Spectroscopy

Fourier transform infrared spectroscopy (FTIR) was used to analyze the chemical structure of a-TiO₂-based NPs [51]. The analyses were performed by the Nicolet 5700 model in transmission mode through a KBr beam splitter. The measurements were made using potassium bromide pellets (KBr, 99+%, FTIR grade from Sigma-Aldrich). The pellets were obtained by finely ground 5 mg of a-TiO₂ based NPs mixed with 200 mg of potassium bromide, and then pressed into a disc.

2.4.4. Ultraviolet-Visible (UV-Vis) Spectroscopy

Absorption properties and photonic bandgap were optically analyzed by UV-Vis absorption spectrophotometry. The UV-Vis spectra were acquired in the range 200–1000 nm through a MultiskanTM FC Microplate Photometer from Thermo Fisher Scientific using the SkanIT RE software. Spectra were background subtracted.

2.4.5. Dynamic Light Scattering (DLS) and Zeta Potential (Z-Potential)

The hydrodynamic diameter and zeta potential (Z-potential) of the a-TiO₂ based NPs were determined by dynamic light scattering (DLS) using a Zetasizer Nano ZS90 from Malvern.

DLS measurements were performed by suspending 500 µg of NPs in 1 mL of bidistilled water. Z-potential measurements were performed in bidistilled water using the same concentration already used for DLS measurements.

2.5. Fluorescence Microscopy Imaging

The a-TiO₂-NH₂ NPs coupled with lipids ready after preparation were characterized through wide-field fluorescence microscopy with colocalization method. The aim of this method is to evaluate the percentage of coupling between lipids and titania NPs. Samples were prepared by withdrawing 10 µL of the lipid-coated a-TiO₂-NH₂ NPs solution and depositing them on the microscope slide; then the drops were covered with a cover-glass slip and this was fixed with a common nail polish. The images were acquired using a wide-field optical fluorescence microscope Nikon Eclipse Ti, equipped with a super-bright wide spectrum Shutter Lambda XL source with a collection of four filter cubes. The images were acquired with 60× and 100× PLAN-APO immersion oil objectives and the data analyzed by the NIS-element software. Amorphous TiO₂-NH₂ NPs labeled with Atto-550 NHS ester dye were used for this purpose and the lipids with DiOC₁₈, as described above. Images were thus acquired by exciting the dyes at two different wavelength channels: 550 nm (red channel) and 488 nm (green channel). The colocalization tool of NIS-Element software (NIS-Elements AR 4.5, Nikon) was used to evaluate the coupling percentages, as previously reported [58,59]: after setting a threshold between 0.1 and 1 µm to disregard larger aggregates, the spots in the red channel (identifying the a-TiO₂-NH₂ NPs) and green channels (corresponding to the lipid bilayer vesicles) were counted and an overlay of the two images was performed, counting only the spots in which the two fluorescences were colocalized. About 600 fluorescent points were analyzed by this automatic routine by applying a dimensional threshold. The percentage of colocalization was then calculated with respect to the MSN channel with the following formula [Equation (1)]:

$$\% \text{TiO}_2 \text{ NPs colocalized} = (n^\circ \text{ a-TiO}_2\text{-NH}_2 \text{ NPs colocalized}) / (n^\circ \text{ a-TiO}_2\text{-NH}_2 \text{ NPs}) \quad (1)$$

2.6. Spin Trapping Measurements Coupled with EPR Spectroscopy

The evaluation of ROS generation under US stimulation was performed by Electron Paramagnetic Resonance (EPR) Spectroscopy through the EMX Nano X-Band Spectrometer from Bruker. The EPR measurements were assisted by a spin-trapping technique and the ROS production due to US stimulation was provided by a commercial apparatus (LipoZero G39 from GLOBUS).

The sonication was performed by placing 1 mL of sample (200 µg/mL NPs concentration) in a 24-well plate from Thermo Scientific which was positioned in contact with the LipoZero transducer. A thin layer of water-based gel (Stosswellen Gel Bestelle from ELvation Medical GmbH) was added to maximize the coupling between the transducer and the plate. The conditions used to stimulate all samples were the following: sonication time 1 min, working frequency 1 MHz, duty cycle 100%, and US output powers of 0.3, 0.6, 0.9, and 1.2 W/cm² (corresponding to 10%, 20%, 30%, and 40% of the maximum output power of the device). After the US stimulation, the sample was immediately transferred into a quartz microcapillary tube and placed in the EPR spectrometer cavity. The production of hydroxyl and superoxide anion radicals was detected in bidistilled water and 5,5-dimethyl-L-pyrroline-N-oxide (DMPO, from Sigma), was used as a spin trap. Before each measurement, DMPO (from a stock solution of 10 mM) was added to each tested sample. The spin trap is essential due to its ability to trap both radicals (hydroxyl and superoxide anion) increasing their lifetime and enabling their measurement by the EPR spectroscopy.

The parameters to collect the EPR spectra were the following: center field 3426 G, sweep time 100.0 s, sample g-factor 2.000, and number of scans 10.

After the acquisition, the spectra were processed through the Bruker Xenon software for baseline correction. Analysis of the recorded data was made using the Bruker SpinFit software.

All EPR experiments were carried out under daylight conditions, except the assays designed to evaluate the eventual synergistic effect between visible light and US stimuli. In this case, output powers of 0.9 and 1.2 W/cm² of US irradiation were used.

Note that no UV stimulation was performed to any of the a-TiO₂-based NPs before any experiment. All EPR experiments were carried out in triplicate.

2.7. Passive Cavitation Detection Experiment

The acoustic cavitation activity caused by the acoustic pressure reached inside the well due to US in the presence or absence of NPs was analyzed by recording the broad band acoustic emissions generated by the collapsing bubbles. For that, a focused piezo-detector used as cavitometer coupled to a spectrum analyzer was used and the signal power was computed from the fast Fourier transform (FFT) for a frequency range of 0.8–5.0 MHz. The US irradiation setup for the measurements was based on the one presented by Vighetto et al. [12]. The only difference is that the 1 cm for tissue-mimicking material was not considered.

In detail, the samples were irradiated with US from the LipoZero G39 instrument for 1 min, at a frequency of 1 MHz. The experiment was carried out for four different output powers (0.3, 0.6, 0.9, and 1.2 W/cm²) and with and without a-TiO₂ based NPs (i.e., a-TiO₂ NPs, a-TiO₂-NH₂ NPs and lipid coated titania, a-TiO₂-NH₂//DOPC-DOTAP) in suspension. During each experiment, samplings of 100 µs each of the acoustic signal (generated by the cavitation phenomena) were recorded every 2 s, corresponding to a total of 30 cycles. The Fourier transform (FT) of the acoustic signal was calculated for each cycle, filtering out all frequencies below 2 MHz, thus removing the frequency components of the stimulus. Finally, the area under the curve of each spectrum was calculated. This area is proportional to the energy release caused by the collapse of the cavitation bubbles.

3. Results

Amorphous TiO₂ based NPs, synthesized at room temperature following a new eco-friendly alkaline sol-gel route, based on some of the authors' previous work [49], were used in this work.

Pristine a-TiO₂ NPs, in situ propylamine functionalized a-TiO₂-NH₂ NPs and biomimetic a-TiO₂ NPs//DOPC-DOTAP (a-TiO₂ NPs coupled with the cationic lipid formulation DOPC-DOTAP) were prepared, characterized, and evaluated as sonosensitizers (to increase ROS generation under US stimulation) through EPR spectroscopy and PCD analysis.

3.1. A-TiO₂ NPs Structural Characterization: TEM, XRD, and FTIR

Amorphous TiO₂ based NPs have been structurally characterized by TEM, XRD, and FTIR by some of the authors [51].

TEM images (Figure 1a) show the spherical morphology and evidence the monosized (static) diameter of around 3–4 nm ± 0.1 nm of a-TiO₂ NPs. The spherical morphology is indicative of the NPs amorphous character [62,63].

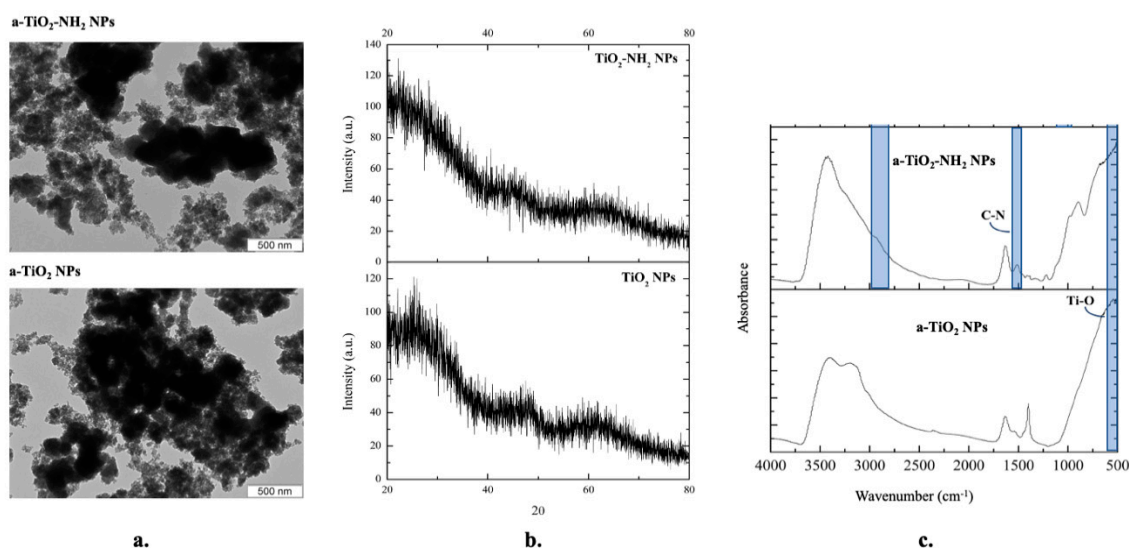


Figure 1. Physical characterization of amorphous TiO₂ (a-TiO₂) (lower panels) and a-TiO₂-NH₂ nanoparticles (NPs) (upper panels): (a) TEM images, (b) X-ray diffractograms, and (c) FTIR spectra.

The amorphous nature of all the synthesized TiO₂ NPs was confirmed through XRD: no defined or sharp peaks were present in diffractograms (Figure 1b).

FTIR spectra (Figure 1c) prove the success of propylamine a-TiO₂ NPs in-situ functionalization. The main FTIR TiO₂ peak (centered at 526 cm⁻¹ and assigned to the stretch of Ti-O-Ti bond) is present in all spectra and identifies the titania network. Concerning the a-TiO₂-NH₂ NPs spectrum, a peak centered at 1510 cm⁻¹ (and assigned to C-N bond) and slight shoulder located at 2940 cm⁻¹ (and assigned to C-H stretching) were identified, proving the amine functionalization.

3.2. Ultraviolet-Visible (UV-Vis) Spectroscopy

The electronic structure of crystalline solids is well established whereby different crystalline forms exhibited different band gap values. In the case of crystalline TiO₂, rutile (the most ordered TiO₂ structure) presents a band gap of ≈3.0 eV while anatase exhibits a higher value of ≈3.23 eV [53,64–66]. Although physical models and mathematical tools developed for crystalline solids are not always valid for amorphous materials, electronic gaps do occur on amorphous materials, and an experimental ≈3.18 eV value was obtained for a-TiO₂ NPs [53].

The UV-Vis spectra for the synthesized a-TiO₂ NPs are shown in Figure 2a. The straight-line extrapolation method and the Tauc's plot (used in the determination of semiconductors bandgap) were used to estimate the light absorption edge and bandgap values (E_g) for the synthesized NPs (Figure 2b,c).

The absorption bands (observed at 369 nm for pristine a-TiO₂ NPs and at 357 nm for a-TiO₂-NH₂ NPs in Figure 2a) are due to the semiconductor excitation and quantum size effects, as reported by Xu et al. [66]. The slight blue shift observed on the absorption band (in comparison with those of anatase at $\lambda = 385$ nm [67]), is attributed to the NPs sizes and morphologies, since the number of photons reaching the NPs core depends on their size and the optical properties [67].

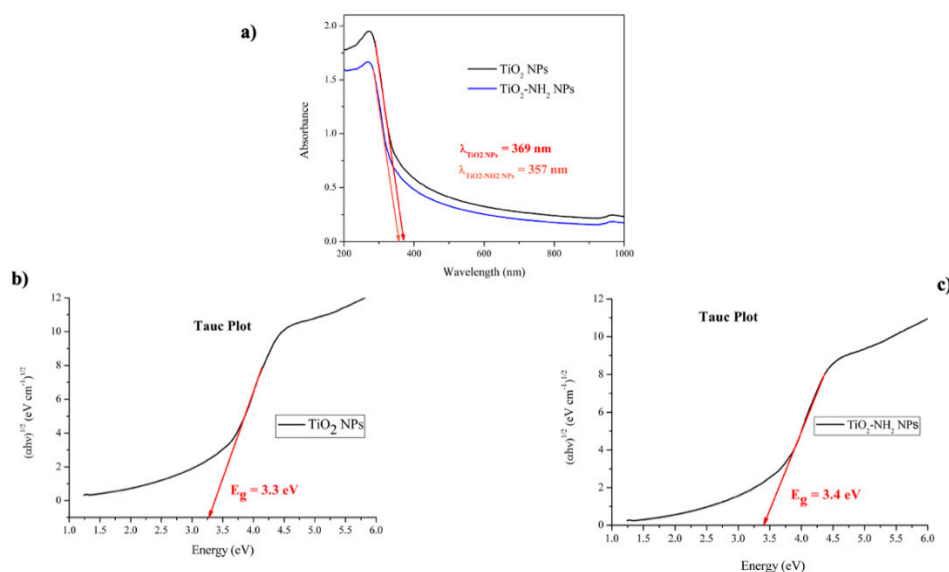


Figure 2. Bandgap energy of a-TiO₂ based NPs: (a) UV-Vis spectra; (b) Tauc's plot of a-TiO₂ indirect band gap; (c) Tauc's plot TiO₂-NH₂ indirect bandgap.

Amorphous-TiO₂ NPs show an experimental E_g value of 3.3 eV, slightly higher than some of the authors' previously obtained values [53]. Unlike crystalline forms, amorphous networks have plenty of structural possibilities which explains the dispersity of experimental bandgap values.

The a-TiO₂-NH₂ NPs experimental E_g value was 3.4 eV (very similar to the pristine a-TiO₂ bandgap value) meaning that the functionalization with the propylamine does not influence the main a-TiO₂ NPs electronic structure.

Moreover, all the obtained experimental bandgaps lie in the UV regime, predicting no daylight stimulation on the synthesized a-TiO₂-based NPs.

3.3. Dynamic Light Scattering (DLS) and Zeta Potential (Z-Potential)

The colloidal stability and the hydrodynamic diameter of the a-TiO₂ based NPs (a-TiO₂, a-TiO₂-NH₂ and a-TiO₂-NH₂//DOPC-DOTAP) were evaluated through Z-potential and DLS (Figure 3).

The Z-potential evidences the surface chemistry on colloidal stability (Figure 3a). Amorphous-TiO₂ NPs present the most negative Z-potential value ($\zeta = -40.0$ mV, outside $|\zeta| \geq \pm 30$ mV risky range) allowing us to conclude about their colloidal stability.

Amine-groups protonation is responsible for the increase in zeta potential of a-TiO₂-NH₂ NPs up to -24.2 mV. Although this value is an indirect proof of amine-functionalization, it also evidences the flocculation and/or coagulation risks associated with these amine-functionalized nanosystems.

Finally, the biomimetic a-TiO₂-NH₂//DOPC-DOTAP NPs present the highest positive Z-potential (69.1 mV, outside the aggregation risk range). This fact proves the effective coupling between the positively charged lipids and a-TiO₂-NH₂ NPs and it is also an evidence of their colloidal stability.

The hydrodynamic diameter evaluation through DLS showed that no micro-scale aggregates were present, which suggests a relatively good dispersion of all the samples (Figure 3b). However, the a-TiO₂-NH₂ NPs suspension (the one within the risky zeta potential range) shows the highest hydrodynamic diameter (centered at ≈ 156.4 nm) and the widest peak size distribution (showing the possibility of aggregation), in accordance to the lowest Z-potential values, as previously discussed. On the other hand, the lipidic shell formation on a-TiO₂-NH₂ NPs contributes to an improvement of sample colloidal dispersion (lowest size distribution diameter, ≈ 43.7 nm, with sharp peak) in accordance with the recorded Z-potential values.

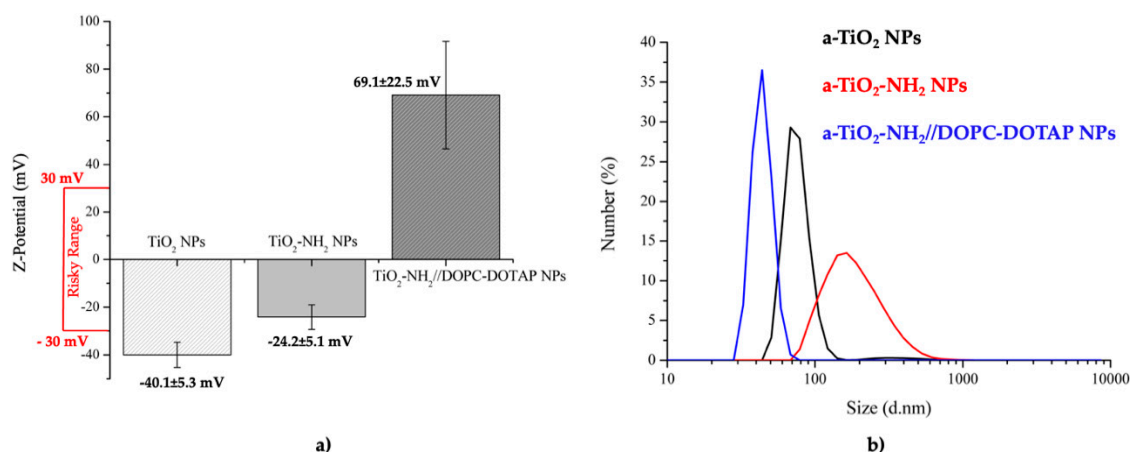


Figure 3. Z-potentials and hydrodynamic diameters of pristine a-TiO₂ NPs, a-TiO₂-NH₂ NPs, and a-TiO₂-NH₂//DOPC-DOTAP NPs suspended in milliQ water: (a) Z-potential measurements; (b) dynamic light scattering measurements in number (%).

3.4. Colocalization Experiments

The formation of the lipid bilayer on the surface of a-TiO₂-NH₂ NPs was confirmed through wide-field fluorescence microscopy colocalization experiments (Figure 4).

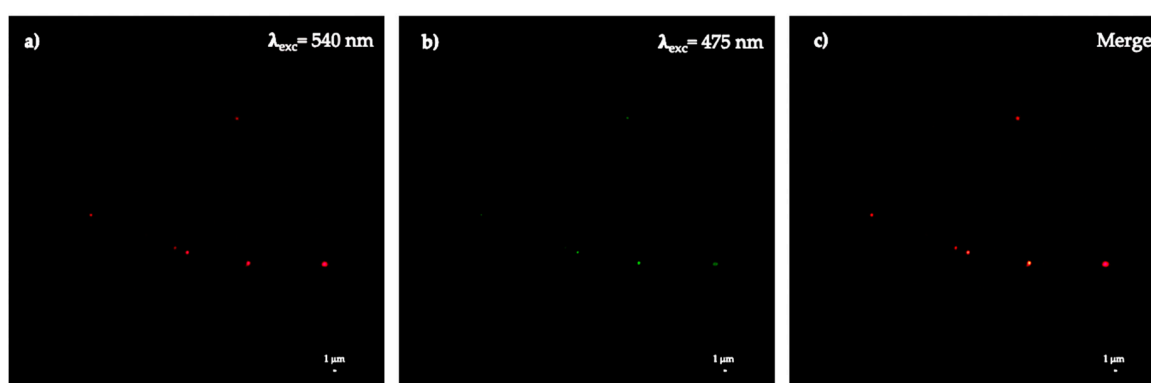


Figure 4. Wide-field fluorescence image of (a) a-TiO₂ NPs labeled with ATTO 550-NH₂ ester; (b) lipid shell labeled with 1% of DiOC₁₈; (c) the merged channels showing complete colocalization. Scale bar: 1 μm and mass ratio NPs:Lipids (1:5).

Two different mass ratios (1.5:5 and 1:5) were tested to achieve the best ratio of NPs:Phospholipids. The obtained results confirm a successful colocalization between the phospholipids and a-TiO₂ NPs for both ratios (Figure 4). The best result was achieved for 1:5 mass ratio with 88.5 ± 13.8% of colocalization (Table 1) between the red spots (coming from the ATTO 550 dye labeling the titania nanoparticles) and the green ones (deriving for the DiO dye coupled with the lipid bilayers) and thus this was the selected ratio to proceed with further experiments (EPR and cavitation).

Table 1. Conjugation yield in percentage obtained for both mass ratio tested of Nanoparticles (NPs):Phospholipids (1:5 and 1.5:5).

	a-TiO ₂ -NH ₂ //DOPC-DOTAP 1:5 (m/m)	a-TiO ₂ -NH ₂ //DOPC-DOTAP 1.5:5 (m/m)
Colocalization (%)	88.54 ± 13.75	75.0 ± 35.6

3.5. EPR Spectroscopy

EPR spectroscopy was used to evaluate the improvement on ROS generation due to the influence of NPs in water, according to different US powers. The samples ($[NPs] = 200 \mu\text{g/mL}$) were irradiated with US for 1 min, at a frequency of 1 MHz, a Duty Cycle of 100%.

Figure 5 reports the EPR spectra after US stimulation of the NPs and clearly shows the presence of characteristics DMPO-OH spin adducts due to the presence of ROS (Figure 5c,d). For output power higher than 0.9 W/cm^2 a qualitative increase in ROS generation was observed when pristine a-TiO_2 and $\text{a-TiO}_2\text{-NH}_2$ NPs were present.

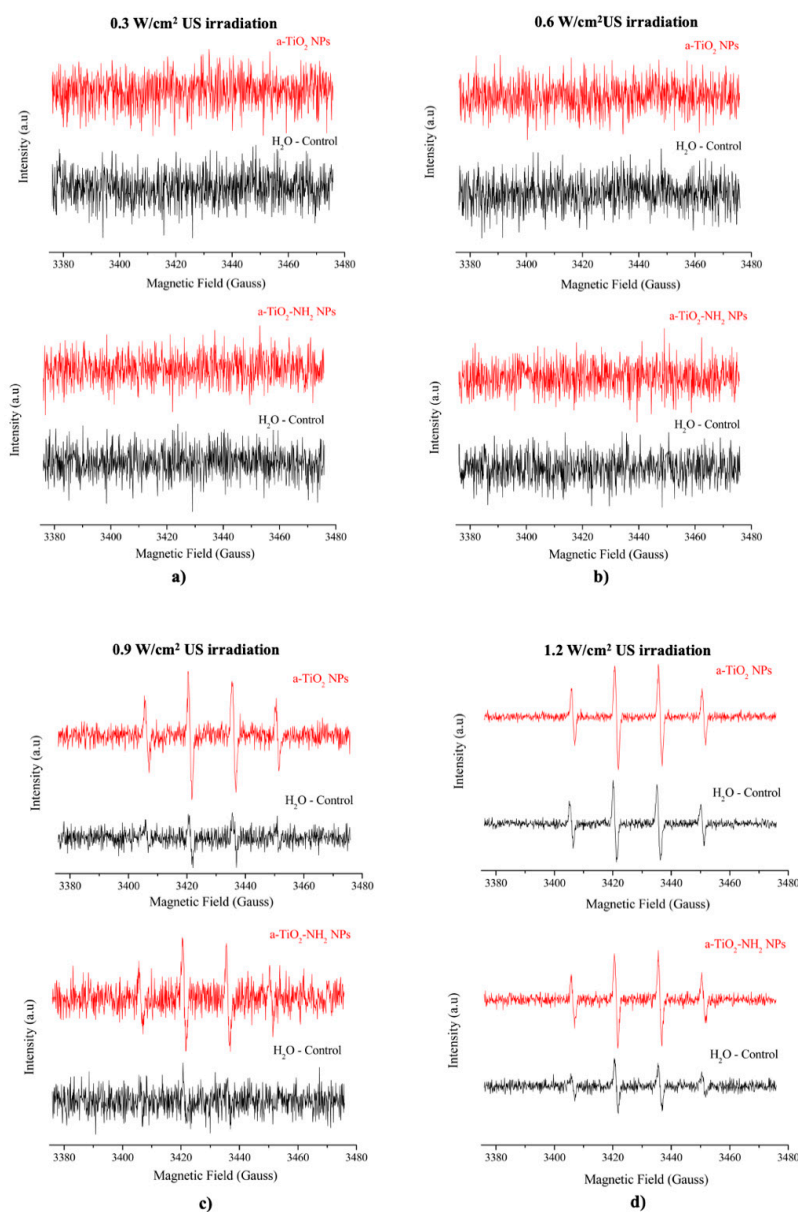


Figure 5. EPR spectra of amine-functionalized (graphs on top) and pristine (graphs on the bottom) a-TiO_2 based NPs ($200 \mu\text{g/mL}$) in water using DMPO (10 mM) as spin trap, irradiated with different US powers: (a) irradiation of 0.3 W/cm^2 of US, (b) irradiation of 0.6 W/cm^2 of US; (c) irradiation of 0.9 W/cm^2 of US; (d) irradiation of 1.2 W/cm^2 of US. Black spectra: control sample—water without NPs; red spectra: water with $200 \mu\text{g/mL}$ of a-TiO_2 based NPs.

For quantitative evaluation, Table 2 shows the concentration of DMPO-OH spin adduct measured in all the analyzed conditions. Those data are directly correlated to ROS production, especially to the hydroxyl and superoxide anions. Concerning both pristine a-TiO₂ and a-TiO₂-NH₂ NPs measured under daylight conditions, an increase in ROS generation was detected for US output powers of 0.9 and 1.2 W/cm².

Table 2. Concentrations of DMPO-OH spin adduct obtained by using Bruker SpinFit software. All the experiments were performed in daylight. In the case of the highest ROS production, i.e., concerning the sample a-TiO₂-NH₂ NPs, tests in dark conditions were also performed.

US Output Power (W/cm ²)	a-TiO ₂ NPs (Daylight Conditions) [·OH] M	a-TiO ₂ -NH ₂ NPs (Daylight Conditions) [·OH] M	a-TiO ₂ -NH ₂ NPs (Dark Conditions) [·OH] M	a-TiO ₂ -NH ₂ //DOPC-DOTAP NPs (Daylight Conditions) [·OH] M
0	-	0	-	-
0.3	0	0	-	0
0.6	0	0	-	0
0.9	1.81×10^{-5}	3.297×10^{-5}	1.73×10^{-6}	0
1.2	1.54×10^{-5}	3.295×10^{-5}	1.98×10^{-5}	0

The EPR spectra of biomimetic a-TiO₂-NH₂//DOPC-DOTAP NPs suspension (Figure 6) show that no generation of ROS occurs, even when the sample is stimulated with the highest values of US irradiation powers (at daylight). In this case, even for US powers for which ROS were detected on the control samples (US powers of 0.9 and 1.2 W/cm²), no ROS production was observed for a-TiO₂-NH₂//DOPC-DOTAP NPs suspension (Figure 6 and Table 2).

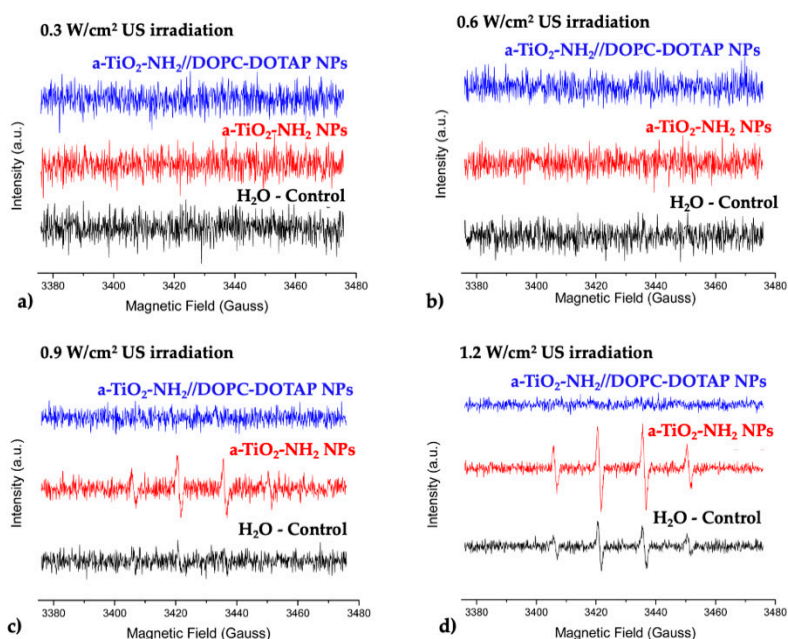


Figure 6. EPR spectra of a-TiO₂-NH₂ based NPs (200 µg/mL) in water using DMPO (10 mM) as spin trap, irradiated with different US powers: (a) 0.3 W/cm² of US output power, (b) 0.6 W/cm² of US output power; (c) 0.9 W/cm² of US output power; (d) 1.2 W/cm² of US output power. Black spectra: control sample—water without NPs; red spectra: water with 200 µg/mL of a-TiO₂-NH₂ NPs; blue spectra: water with 200 µg/mL of a-TiO₂-NH₂//DOPC-DOTAP NPs.

Although all the synthesized a-TiO₂ based NPs exhibited band gaps in the UV region, the influence of visible light on ROS generation was studied. This evaluation was carried out only for the highest responses (corresponding to the highest values of US irradiation, i.e., 0.9 and 1.2 W/cm², see Table 2).

The obtained results evidence a synergistic effect between daylight and US irradiation (Figure 7). As control, a sample containing α -TiO₂-NH₂ NPs was analyzed after being exposed to visible light without any US stimulation and actually no ROS detection was observed (Figure 7 (1)). Thus, visible light alone is not sufficient to enable the ROS generation from α -TiO₂-NH₂ NPs, while US irradiation and visible light seem to have a synergistic effect by increasing the generation of ROS with respect to US stimulation only (Figure 7 (2)).

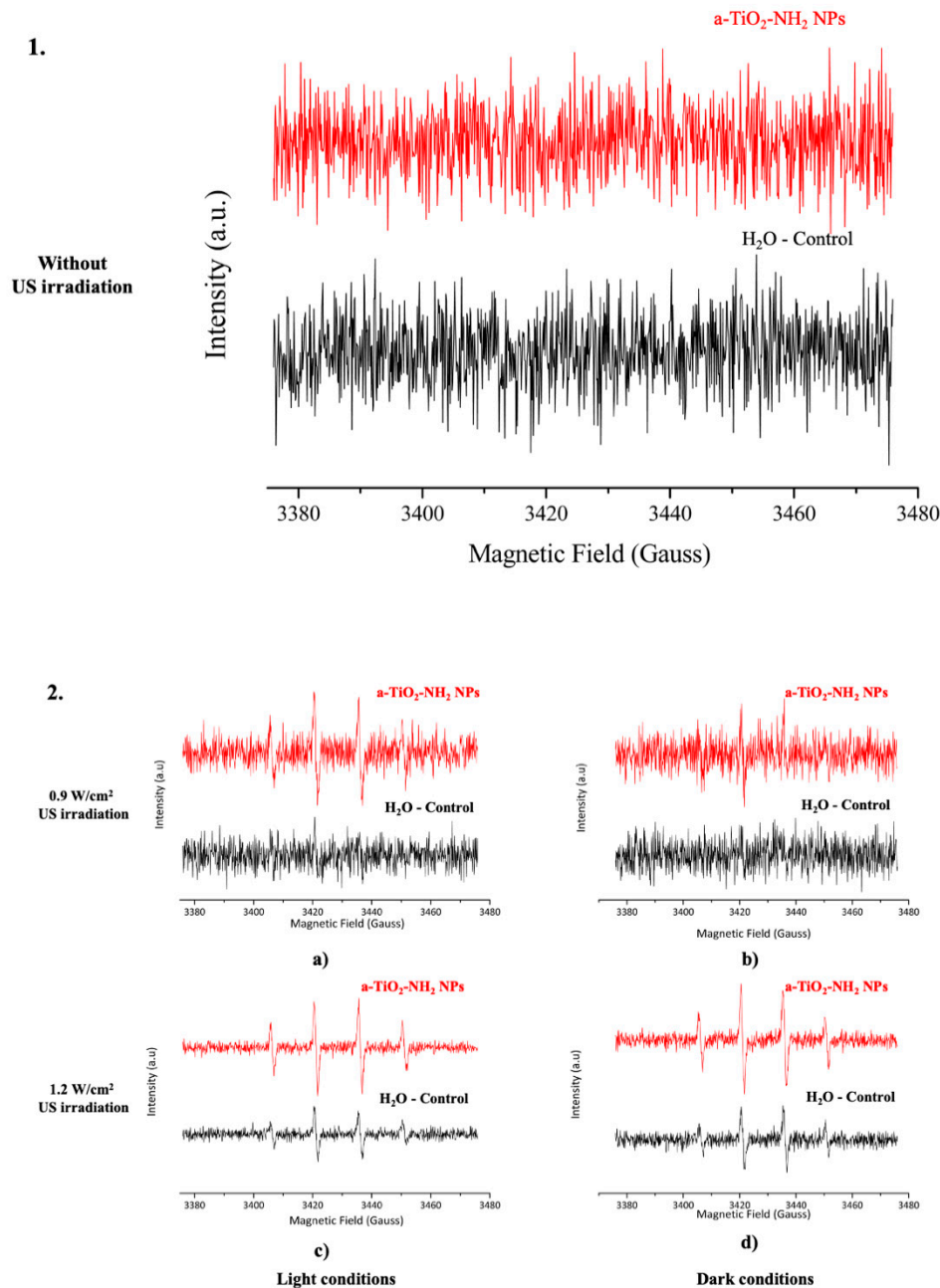


Figure 7. Influence of visible light and US stimulation on ROS production. **1.** EPR spectra of α -TiO₂-NH₂ NPs (200 μ g/mL) in water using DMPO (10 mM) as spin trap, experiment performed at daylight without US irradiation; **2.** EPR spectra of α -TiO₂-NH₂ NPs (200 μ g/mL) in water using DMPO (10 mM) as spin trap, irradiated with different US powers—0.9 W/cm² of US output power in: (a) daylight conditions and (b) dark conditions; and at 1.2 W/cm² of US output power in (c) daylight conditions and (d) dark conditions. Black spectra: control sample—water without NPs; red spectra: water with 200 μ g/mL of α -TiO₂-NH₂ NP.

3.6. Passive Cavitation Detection

The evaluation of the acoustic cavitation on the generation of ROS after US exposure was performed through passive cavitation detection (PCD) technique. The experiments allowed us to measure the acoustic pressures reached inside the well for all the samples and the conditions tested. More details about the experiment execution and data interpretation are reported in the Materials and Method section.

Figure 8 shows the area under the curve for all cycles at different US powers with and without a-TiO₂ based NPs (a-TiO₂ NPs and a-TiO₂-NH₂ NPs) in suspension. This area is proportional to the energy release caused by the collapse of the cavitation bubbles.

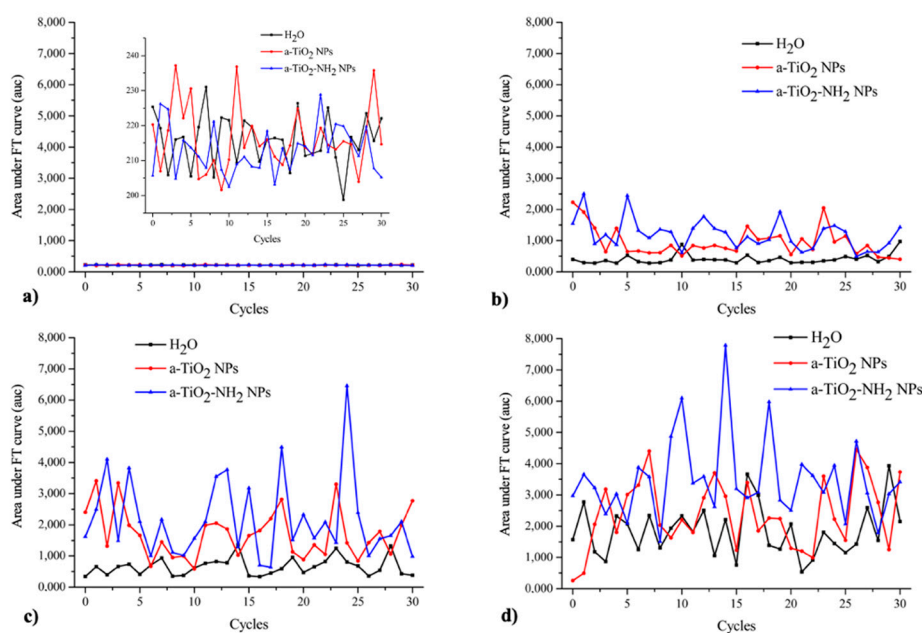


Figure 8. Area under the FT curve computed from the signal recorded through a focused piezo-detector used as cavitometer to analyze the cavitation of water and a-TiO₂ based NPs suspensions. The analysis were made using the following conditions: 1 MHz, 100% of DC, 1 min of irradiation with (a) 0.3 W/cm² of US output power; (b) 0.6 W/cm² of US output power; (c) 0.9 W/cm² of US output power; (d) 1.2 W/cm² output power.

Figure 8 shows the obtained frequency spectra of the acoustic signals at different US intensities with and without a-TiO₂ based NPs (a-TiO₂ NPs and a-TiO₂-NH₂ NPs) in suspension.

It can be observed that only harmonics and subharmonics are present in all sample types, i.e., both water and water with pristine and amine-functionalized a-TiO₂ NPs when the samples were irradiated by the lowest US power (0.3 W/cm²). These signals are probably due to the oscillation of large gas bubbles trapped in the plastic wells of the sample holder. For 0.6 and 0.9 W/cm² powers, as shown in Figure 8b,c, an acoustic broadband noise was recorded in case of a-TiO₂ based NPs samples. This acoustic broadband corresponds to the inertial cavitation occurrence. On the other hand, in presence of water solution without NPs, the acoustic broadband noise was only detected when the sample was irradiated with the highest US power tested, 1.2 W/cm² (Figure 8d). These results allow us to conclude that the a-TiO₂ based NPs act as nucleation sites inducing inertial cavitation. The decrease of the threshold of US power needed to cause the collapse of the induced cavitation bubbles, enables the generation of sufficiently high temperatures and pressures to ROS production, even at low US power [12].

A comparison between these results and those obtained through EPR spectroscopy can be carried out. The US power threshold needed to induce passive cavitation, and thus the ROS generation,

is different. Indeed, the passive cavitation detection (PCD) can be considered a more sensitive technique if compared to EPR spectroscopy.

Interestingly, in the case of the a-TiO₂-NH₂ NPs coupled with lipids, the signal difference between the control sample (water without NPs) and the a-TiO₂-NH₂//DOPC-DOTAP NPs sample is even more pronounced (Figure 9).

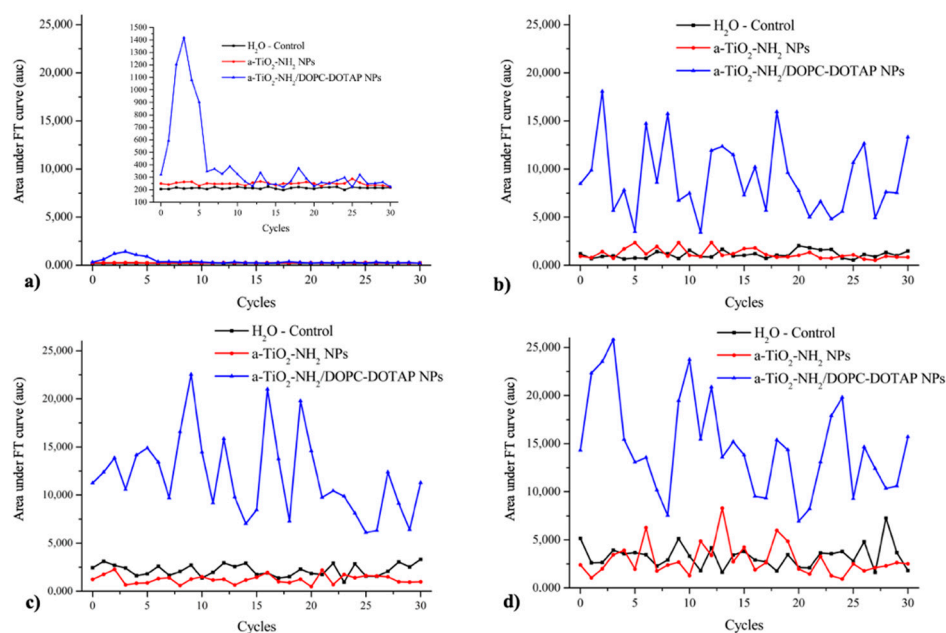


Figure 9. Area under the FT curve computed from the signal recorded through a focused piezo-detector used as cavimeter to analyze the cavitation of water and a-TiO₂-NH₂ based NPs suspensions. The analyses were performed using the following conditions: 1 MHz, 100% of DC, 1 min of irradiation with (a) 0.3 W/cm² of US output power; (b) 0.6 W/cm² of US output power; (c) 0.9 W/cm² of US output power; (d) 1.2 W/cm² output power.

In this case, the acoustic broadband noise was recorded for all the tested powers (0.3, 0.6, 0.9, and 1.2 W/cm²), being more pronounced from 0.6 W/cm². These results show that the a-TiO₂-NH₂//DOPC-DOTAP NPs could act as a promising cavitation enhancer nano-agent, if compared to other already analyzed NPs (pristine a-TiO₂ NPs and a-TiO₂-NH₂ NPs). This is a more stable suspension (see Section 3.3) and is able to decrease even more the threshold of US power needed to occur the collapse of the induced cavitation bubbles, which directly influence the generation of ROS. However, it is important to mention that the presence of the lipidic bilayer is able to scavenge the generated ROS, which are in fact not detectable by the EPR characterization.

In this case, the possible future mechanism of cytotoxicity should be also evaluated, as it will not rely on ROS generation, but on mechanical effects. For example, the “nanoscalpel effect” can be mentioned, since some of the authors recently demonstrated it as an effective killing mechanism of cancer cells *in vitro* when irradiating other semiconductor nanocrystals, zinc oxide, with ultrasound [68].

4. Discussion

The aim of this work was to analyze the ability of a-TiO₂ based NPs (a-TiO₂, a-TiO₂-NH₂ NPs) to act as ultrasound responding agents to improve the generation of ROS and/or act as a cavitation enhancer for biomedical applications, namely, to fight cancer cells.

The developed a-TiO₂ NPs were synthesized for the first time through a novel, room-temperature, base-catalyzed sol-gel protocol. Furthermore, to improve the colloidal stability of the developed NPs, a new biomimetic coating based on double lipidic bilayer, self-assembled on the NPs, was performed.

To analyze the generation of ROS and cavitation in the tested suspensions after US stimuli, two different techniques were used, respectively: electron paramagnetic resonance (EPR) spectroscopy and passive cavitation detection (PCD). The concentration of the NPs suspensions was kept constant only varying the output powers of US irradiation. The EPR spectroscopy and PCD results agree and both suggest that the a-TiO₂ and a-TiO₂-NH₂ NPs are promising candidates to US responding agents, since the generation of ROS increases when in presence of the a-TiO₂ based NPs. Another studied parameter was the influence of visible light. The obtained results allow us to conclude that a synergistic effect exists between the ultrasounds and visible light when the samples are exposed to both stimuli.

The colloidal stability and dispersibility improvement of the a-TiO₂ based NPs were also investigated, since the high aggregation tendency in water and physiological media can make the application of TiO₂ NPs unfeasible to biological systems [49,50,56]. Thus, the a-TiO₂-NH₂ NPs were coupled with DOPC-DOTAP phospholipids and the obtained results were very encouraging since stable colloidal suspensions with very high conjugation yield ($\approx 88\%$) were achieved. Biomimetic a-TiO₂-NH₂//DOPC-DOTAP NPs were also analyzed through EPR and PCD. The PCD results suggest that the threshold of US power needed to cause the collapse of the induced cavitation bubbles (which influence directly the generation of ROS) is lower than what previously observed for the a-TiO₂ NPs and a-TiO₂-NH₂ NPs. The absence of detected ROS by EPR measurements in the a-TiO₂-NH₂//DOPC-DOTAP NPs was thus attributed to the scavenging capability of the phospholipid bilayer. As mentioned above, the absence of detected ROS from lipid-coated a-TiO₂ NPs is not related to the cavitation effect. In contrast, these nanoparticles showed enhanced cavitation in water solutions once irradiated by US. For this reason, such biomimetic nanoparticles still represent a promising nanotherapeutic tool against cancer, as recent studies have shown anyway the cytotoxic activity induced by cavitation only once nanoparticles are present [68] and have demonstrated this therapeutic effect in absence of generated ROS.

We conclude that our study proposes a modulating nanoplatform for cancer therapy where enhanced inertial cavitation or enhanced ROS production can be selectively preferred depending on the sample formulation and chemical surface functionalization.

Author Contributions: Conceptualization, J.C.M., L.C.J.P., J.C.W. and V.C.; methodology, M.L., M.C.G. and V.C.; software, V.V.; validation, M.L. and V.V.; investigation, J.C.M. and V.V.; resources, M.C.G. and V.C.; data curation, J.C.M., M.L. and V.V.; writing—original draft preparation, J.C.M.; writing—review and editing, M.L., V.V., M.C.G., V.C.; supervision, M.L., L.C.J.P., J.C.W., M.C.G. and V.C.; project administration, M.C.G. and V.C.; funding acquisition, M.C.G. and V.C. All authors have read and agreed to the published version of the manuscript.

Funding: This research was partially funded by Foundation for Science and Technology (FCT) Portugal, grant numbers UID/Multi/04349/2013 and UID/QUI/00100/2013, and partially received funding from the European Research Council (ERC) under the European Union's Horizon 2020 research and innovation program (grant agreement no. 678151—project acronym. "TROJANANOHORSE"—ERC starting grant).

Acknowledgments: J.C. Matos gratefully acknowledges Foundation for Science and Technology (FCT) ChemMat doctoral program (PD/BD/127914/2016).

Conflicts of Interest: The authors declare no conflict of interest.

References

1. WHO Cancer. Available online: www.who.int/cancer/en/ (accessed on 4 May 2020).
2. Bhatt, A.P.; Redinbo, M.R.; Bultman, S.J. The role of the microbiome in cancer development and therapy. *CA Cancer J. Clin.* **2017**, *67*, 326–344. [CrossRef]
3. Pitot, H. *Fundamentals of Oncology*; Marcel Dekker: New York, NY, USA, 1978.
4. Matsumura, Y.; Maeda, H. A new concept for macromolecular therapeutics in cancer chemotherapy: Mechanism of tumorotropic accumulation of proteins and the antitumor agent smancs. *Cancer Res.* **1986**, *46 Pt 1*, 6387–6392.
5. Gerlowski, L.E.; Jain, R.K. Microvascular permeability of normal and neoplastic tissues. *Microvasc. Res.* **1986**, *31*, 288–305. [CrossRef]

6. Wilhelm, S.; Tavares, A.J.; Dai, Q.; Ohta, S.; Audet, J.; Dvorak, H.F.; Chan, W.C.W. Analysis of nanoparticle delivery to tumours. *Nat. Rev. Mater.* **2016**, *1*, 16014. [[CrossRef](#)]
7. Overchuk, M.; Zheng, G. Overcoming obstacles in the tumor microenvironment: Recent advancements in nanoparticle delivery for cancer theranostics. *Biomaterials* **2018**, *156*, 217–237. [[CrossRef](#)] [[PubMed](#)]
8. Vallet-Regí, M.; Colilla, M.; Izquierdo-Barba, I.; Manzano, M. Mesoporous Silica Nanoparticle for Drug Delivery: Current insights. *Molecules* **2018**, *23*, 47. [[CrossRef](#)] [[PubMed](#)]
9. Barui, S.; Cauda, V. Multimodal decorations of mesoporous silica nanoparticles for improved cancer therapy. *Pharmaceutics* **2020**, *12*, 527. [[CrossRef](#)] [[PubMed](#)]
10. Gonçalves, M.C. Sol-Gel Silica Nanoparticles in Medicine: A Natural Choice. Design, Synthesis and Products. *Molecules* **2018**, *23*, 2021. [[CrossRef](#)]
11. Racca, L.; Cauda, V. Remotely-activated nanoparticles for anticancer therapy. *Nano Micro Lett.* **2021**, *13*, 1–34. [[CrossRef](#)]
12. Vighetto, V.; Ancona, A.; Racca, L.; Limongi, T.; Troia, A.; Canavese, G.; Cauda, V. The synergistic effect of nanocrystals combined with ultrasound in the generation of reactive oxygen species for biomedical applications. *Front. Bioeng. Biotechnol.* **2019**, *7*, 374. [[CrossRef](#)]
13. Nogueira, V.; Hay, N. Molecular pathways: Reactive oxygen species homeostasis in cancer cells and implications for cancer therapy. *Clin. Cancer Res.* **2013**, *19*, 4309–4314. [[CrossRef](#)] [[PubMed](#)]
14. Tong, L.; Chuang, C.C.; Wu, S.; Zuo, L. Reactive oxygen species in redox cancer therapy. *Cancer Lett.* **2015**, *367*, 18–25. [[CrossRef](#)] [[PubMed](#)]
15. Ancona, A.; Dumontel, B.; Garino, N.; Demarco, B.; Chatzitheodoridou, D.; Fazzini, W.; Engelke, H.; Cauda, V. Lipid-Coated Zinc Oxide Nanoparticles as Innovative ROS-Generators for Photodynamic Therapy in Cancer Cells. *Nanomaterials* **2018**, *8*, 143. [[CrossRef](#)] [[PubMed](#)]
16. Dos Santos, A.F.; de Almeida, D.R.Q.; Terra, L.F.; Baptista, M.S.; Labriola, L. Photodynamic therapy in cancer treatment—An update review. *J. Cancer Metastasis Treat* **2019**, *5*, 25. [[CrossRef](#)]
17. Hu, Y.; Masamune, K. Flexible laser endoscope for minimally invasive photodynamic diagnosis (PDD) and therapy (PDT) toward efficient tumor removal. *Opt. Express* **2017**, *25*, 16795–16812. [[CrossRef](#)]
18. Rosenthal, I.; Sostaric, J.Z.; Riesz, P. Sonodynamic therapy—A review of the synergistic effects of drugs and ultrasound. *Ultrason. Sonochem.* **2004**, *11*, 349–363. [[CrossRef](#)]
19. Yumita, N.; Nishigaki, R.; Umemura, K.; Umemura, S.I. Hematoporphyrin as a sensitizer of cell-damaging effect of ultrasound. *Jpn. J. Cancer Res.* **1989**, *80*, 219–222. [[CrossRef](#)]
20. Son, S.; Kim, J.H.; Wang, X.; Zhang, C.; Yoon, S.A.; Shin, J.; Sharma, A.; Lee, M.H.; Cheng, L.; Wu, J.; et al. Multifunctional sonosensitizers in sonodynamic cancer therapy. *Chem. Soc. Rev.* **2020**, *49*, 3244–3261. [[CrossRef](#)]
21. Canavese, G.; Ancona, A.; Racca, L.; Canta, M.; Dumontel, B.; Barbaresco, F.; Limongi, T.; Cauda, V. Nanoparticle-assisted ultrasound: A special focus on sonodynamic therapy against cancer. *Chem. Eng. J.* **2018**, *340*, 155–172. [[CrossRef](#)]
22. Harada, Y.; Ogawa, K.; Irie, Y.; Endo, H.; Feril, L.B.; Uemura, T.; Tachibana, K. Ultrasound activation of TiO₂ in melanoma tumors. *J. Control. Release* **2011**, *149*, 190–195. [[CrossRef](#)]
23. Yasuda, J.; Miyashita, T.; Taguchi, K.; Yoshizawa, S.; Umemura, S.I. Quantitative assessment of reactive oxygen sonochemically generated by cavitation bubbles. *Jpn. J. Appl. Phys.* **2015**, *54*, 07KF24. [[CrossRef](#)]
24. Qian, X.; Zheng, Y.; Chen, Y. Micro/nanoparticle-augmented sonodynamic therapy (SDT): Breaking the depth shallow of photoactivation. *Adv. Mater.* **2016**, *28*, 8097–8129. [[CrossRef](#)] [[PubMed](#)]
25. Wang, X.; Zhong, X.; Gong, F.; Chao, Y.; Cheng, L. Newly developed strategies for improving sonodynamic therapy. *Mater. Horiz.* **2020**, *7*, 2028–2046. [[CrossRef](#)]
26. Canaparo, R.; Foglietta, F.; Giuntini, F.; Francovich, A.; Serpe, L. The bright side of sound: Perspectives on the biomedical application of sonoluminescence. *Photochem. Photobiol. Sci.* **2020**, *19*, 1114–1121. [[CrossRef](#)] [[PubMed](#)]
27. Yan, X.; Li, Y.; Xia, T. Black Titanium Dioxide Nanomaterials in Photocatalysis. *Int. J. Photoenergy* **2017**, *2017*, 8529851. [[CrossRef](#)]
28. Fagan, R.; McCormack, D.E.; Dionysiou, D.D.; Pillai, S.C. A review of solar and visible light active TiO₂ photocatalysis for treating bacteria, cyanotoxins and contaminants of emerging concern. *Mater. Sci. Semicond. Process.* **2016**, *42*, 2–14. [[CrossRef](#)]

29. Etacheri, V.; Valentin, C.D.; Schneider, J.; Bahnemann, D.; Pillai, S.C. Visible-light activation of TiO₂ photocatalysts: Advances in theory and experiments. *J. Photochem. Photobiol. C* **2015**, *25*, 1–29. [[CrossRef](#)]
30. Pelaez, M.; Nolan, N.; Pillai, S.; Seery, M.; Falaras, P. A review on the visible light active titanium dioxide photocatalysis for environmental applications. *Appl. Catal. B* **2012**, *125*, 331–349. [[CrossRef](#)]
31. Hernández, S.; Cauda, V.; Chiodoni, A.; Dallorto, S.; Sacco, A.; Hidalgo, D.; Celasco, E.; Pirri, C.F. Optimization of 1D ZnO@TiO₂ Core–Shell Nanostructures for Enhanced Photoelectrochemical Water Splitting under Solar Light Illumination. *ACS Appl. Mater. Interfaces* **2014**, *6*, 12153–12167. [[CrossRef](#)]
32. Tianyi, W.; Haitao, J.; Long, W.; Qinfu, Z.; Tongying, J.; Bing, W.; Siling, W. Potential application of functional porous TiO₂ nanoparticles in light-controlled drug release and targeted drug delivery. *Acta Biomater.* **2015**, *13*, 354–363.
33. Jin, X.; Xiaobo, P.; Mengyan, W.; Jiong, M.; Yiyan, F.; Pei-Nan, W.; Lan, M. The role of surface modification for TiO₂ nanoparticles in cancer cells. *Colloids Surf. B Biointerfaces* **2016**, *143*, 148–155.
34. Rehman, F.U.; Zhao, C.; Jiang, H.; Wang, X. Biomedical applications of nano-titania in theranostics and photodynamic therapy. *Biomater. Sci.* **2016**, *4*, 40–54. [[CrossRef](#)] [[PubMed](#)]
35. Bogdan, J.; Plawinska-Czarnak, J.; Zarzynska, J. Nanoparticles of Titanium and Zinc Oxides as Novel Agents in Tumor Treatment: A review. *Nanoscale Res. Lett.* **2017**, *12*, 225. [[CrossRef](#)] [[PubMed](#)]
36. Yamaguchi, S.; Kobayashi, H.; Narita, T.; Kanehira, K.; Sonezaki, S.; Kudo, N.; Kubota, Y.; Terasaka, S.; Houkin, K. Sonodynamic therapy using water-dispersed TiO₂ polyethylene glycol compound on glioma cells: Comparison of cytotoxic mechanism with photodynamic therapy. *Ultrason. Sonochem.* **2011**, *18*, 1197–1204. [[CrossRef](#)] [[PubMed](#)]
37. Zhang, H.; Banfield, J.F. Understanding Polymorphic Phase Transformation Behavior during Growth of Nanocrystalline Aggregates: Insights from TiO₂. *J. Phys. Chem. B* **2000**, *104*, 3481–3487. [[CrossRef](#)]
38. Ranade, M.R.; Navrotsky, A.; Zhang, H.Z.; Banfield, J.F.; Elder, S.H.; Zaban, A.; Borse, P.H.; Kulkarni, S.K.; Doran, G.S.; Whitfield, H.J. Energetics of nanocrystalline TiO₂. *Proc. Natl. Acad. Sci. USA* **2002**, *99*, 6476–6481. [[CrossRef](#)]
39. Zhang, H.Z.; Chen, B.; Banfield, J.F. Atomic structure of nanometer-sized amorphous TiO₂. *Phys. Rev. B* **2008**, *78*, 214106. [[CrossRef](#)]
40. Hoang, V.V. Atomic mechanism of vitrification process in simple monatomic nanoparticles. *Eur. Phys. J. D* **2011**, *61*, 627–635. [[CrossRef](#)]
41. Hoang, V.V.; Ganguli, D. Amorphous nanoparticles—Experiments and computer simulations. *Phys. Rep.* **2012**, *518*, 81–140. [[CrossRef](#)]
42. Hoang, V.V. Structural properties of simulated liquid and amorphous TiO₂. *Phys. Status Solid B* **2007**, *244*, 1280–1287. [[CrossRef](#)]
43. Hoang, V.V.; Zung, H.; Trong, N.H.B. Structural properties of amorphous TiO₂ nanoparticles. *Eur. Phys. J. D* **2007**, *44*, 515–524. [[CrossRef](#)]
44. Feldman, C.; Moorjani, K. Amorphous Semiconductors. *Johns Hopkins APL Tech. Dig.* **1968**, *7*, 2–9.
45. Xiong, H.; Slater, M.D.; Balasubramaniam, M.; Johnson, C.S.; Rajh, T. Amorphous TiO₂ Nanotube Anode for rechargeable sodium ion batteries. *J. Phys. Chem. Lett.* **2011**, *2*, 2560–2565. [[CrossRef](#)]
46. Fritzche, H. Optical and Electrical energy gaps in amorphous semiconductors. *J. Non-Cryst. Solids* **1971**, *6*, 49–71. [[CrossRef](#)]
47. Kanna, M.; Wongnawa, S.; Buddee, S.; Dilokkhunakul, K.; Pinpithak, P. Amorphous titanium dioxide: A recyclable dye remover for water treatment. *J. Sol-Gel Sci. Technol.* **2010**, *53*, 162–170. [[CrossRef](#)]
48. Jeong, Y.-M.; Lee, J.-K.; Jun, H.-W.; Kim, G.-R.; Choe, Y. Preparation of super-hydrophilic amorphous titanium dioxide thin film via PECVD process and its application to dehumidifying heat exchangers. *J. Ind. Eng. Chem.* **2009**, *15*, 202–206. [[CrossRef](#)]
49. Qin, Y.; Sun, L.; Li, X.; Cao, Q.; Wang, H.; Tang, X.; Ye, L. Highly water dispersible TiO₂ nanoparticles for doxorubicin delivery: Effect of loading mode on therapeutic efficacy. *J. Mater. Chem.* **2011**, *21*, 18003–18010. [[CrossRef](#)]
50. Koch, S.; Kessler, M.; Mandel, K.; Dembski, K.; Heuze, S.; Hackenberg, S. Polycarboxylate ethers: The key towards non-toxic TiO₂ nanoparticles stabilisation in physiological solutions. *Colloid Surf. B* **2016**, *143*, 7–14. [[CrossRef](#)]
51. Matos, J.C.; Oliveira, C.; Gonçalves, M.C. Daylight Bactericidal Titania Textiles: A contribution to Nosocomial Infections Control. *Molecules* **2019**, *24*, 1891. [[CrossRef](#)]

52. Peixoto, I.; Faria, M.; Gonçalves, M.C. Synthesis and characterization of novel integral asymmetric monophasic cellulose-acetate/silica/titania and cellulose-acetate/titania membranes. *Membranes* **2020**, *10*, 195. [[CrossRef](#)]
53. Gonçalves, M.C.; Pereira, J.C.; Matos, J.C.; Vasconcelos, H.C. Photonic band gap and bactericide performance of amorphous sol-gel titania: An Alternative to crystalline TiO₂. *Molecules* **2018**, *23*, 1677. [[CrossRef](#)] [[PubMed](#)]
54. Ancona, A.; Troia, A.; Garino, N.; Dumontel, B.; Cauda, V.; Canavese, G. Leveraging re-chargeable nanobubbles on amine-functionalized ZnO nanocrystals for sustained ultrasound cavitation towards echographic imaging. *Ultrason. Sonochem.* **2020**, *67*, 105132. [[CrossRef](#)] [[PubMed](#)]
55. Sviridov, A.P.; Osminkina, L.A.; Nikolaev, A.L.; Kudryavtsev, A.A.; Vasiliev, A.N.; Timoshenko, V.Y. Lowering of the cavitation threshold in aqueous suspensions of porous silicon nanoparticles for sonodynamic therapy applications. *Appl. Phys. Lett.* **2015**, *107*, 123107. [[CrossRef](#)]
56. Limongi, T.; Canta, M.; Racca, L.; Ancona, A.; Vighetto, V.; Tritta, S.; Cauda, V. Improving dispersal of therapeutic nanoparticles in the human body. *Nanomedicine* **2019**, *14*, 797–801. [[CrossRef](#)] [[PubMed](#)]
57. Cauda, V.; Engelke, H.; Sauer, A.; Arcizet, D.; Bräuchle, C.; Rädler, J.; Bein, T. Colchicine-loaded lipid bilayer-coated 50 nm mesoporous nanoparticles efficiently induce microtubule depolymerization upon cell uptake. *Nano Lett.* **2010**, *10*, 2484–2492. [[CrossRef](#)] [[PubMed](#)]
58. Dumontel, B.; Canta, M.; Engelke, H.; Chiodoni, A.; Racca, L.; Ancona, A.; Limongi, T.; Canavese, G.; Cauda, V. Enhanced Biostability and Cellular Uptake of Zinc Oxide Nanocrystals Shielded with Phospholipid Bilayer. *J. Mater. Chem. B* **2017**, *5*, 8799–8813. [[CrossRef](#)] [[PubMed](#)]
59. Dumontel, B.; Susa, F.; Limongi, T.; Canta, M.; Racca, L.; Chiodoni, A.; Garino, N.; Chiabotto, G.; Centomo, M.L.; Pignochino, Y.; et al. ZnO nanocrystals shuttled by extracellular vesicles as effective trojan nano-horses against cancer cells. *Nanomedicine* **2019**, *14*, 2815–2833. [[CrossRef](#)]
60. Illes, B.; Hirschle, P.; Barnert, S.; Cauda, V.; Wuttke, S.; Engelke, H. Exosome-Coated Metal Organic Framework Nanoparticles: An Efficient Drug Delivery Platform. *Chem. Mater.* **2017**, *29*, 8042–8046. [[CrossRef](#)]
61. Ploetz, E.; Zimpel, A.; Cauda, V.; Bauer, D.; Lamb, D.C.; Haisch, C.; Zahler, S.; Vollmar, A.M.; Wuttke, S.; Engelke, H. Metal-Organic Framework Nanoparticles Induce Pyroptosis in Cells Controlled by the Extracellular pH. *Adv. Mater.* **2020**, *32*, 1–8. [[CrossRef](#)]
62. Gonçalves, M.C. Nanomaterials. In *Materials for Construction and Civil Engineering: Science, Processing, and Design*; Gonçalves, M.C., Margarido, F., Eds.; Springer: Berlin/Heidelberg, Germany, 2015; pp. 629–677.
63. Lei, Y.; Zhang, L.D.; Fan, J.C. Fabrication, characterization and Raman study of TiO₂ nanowire arrays prepared by anodic oxidative hydrolysis of TiCl₃. *Chem. Phys. Lett.* **2001**, *338*, 231–236. [[CrossRef](#)]
64. Mogyorosi, K.; Dekany, I.; Fendler, J.H. Preparation and characterization of clay mineral intercalated titanium dioxide nanoparticles. *Langmuir* **2003**, *19*, 2938–2946. [[CrossRef](#)]
65. Wang, T.; Wang, H.; Xu, P.; Zhao, X.; Liu, Y.; Chao, S. The effect of properties of semiconductor oxide films on photocatalytic decomposition of dyeing wastewater. *Thin Solid Films* **1998**, *334*, 103–108. [[CrossRef](#)]
66. Xu, W.; Zhu, S.; Fu, X.C. The growth of TiO_{2-x} film and the quantum size effect studied by UV-Vis spectroscopy, SEM, TEM and AB initio calculation. *J. Phys. Chem. Solids* **1998**, *59*, 1647.
67. Hema, M.; Arasi, A.Y.; Servi, P.T.; Anbarasan, R. Titania Nanoparticles Synthesized by Sol-gel Technique. *Chem. Sci. Trans.* **2013**, *2*, 239–245. [[CrossRef](#)]
68. Racca, L.; Limongi, T.; Vighetto, V.; Dumontel, B.; Ancona, A.; Canta, M.; Canavese, G.; Garino, N.; Cauda, V. Zinc Oxide nanocrystals and high-energy shock waves: A new synergy for the treatment. *Front. Bioeng. Biotechnol.* **2020**, *8*, 577. [[CrossRef](#)]

Publisher's Note: MDPI stays neutral with regard to jurisdictional claims in published maps and institutional affiliations.



© 2020 by the authors. Licensee MDPI, Basel, Switzerland. This article is an open access article distributed under the terms and conditions of the Creative Commons Attribution (CC BY) license (<http://creativecommons.org/licenses/by/4.0/>).